TrasMuon: Trust-Region Adaptive Scaling for Orthogonalized Momentum Optimizers

Peng Cheng [*1] **Jiucheng Zang** [2] **Qingnan Li** [1] **Liheng Ma** [1] **Jimmy Jian** [1] **Boxing Chen** [1] **Yingxue Zhang** [1] **Yufei Cui** [1] **Wen Tong** [1]

arXiv:2602.13498v1 [cs.LG] 13 Feb 2026

Abstract

Muon-style optimizers leverage Newton-Schulz (NS) iterations to orthogonalize updates, yielding update geometries that often outperform Adam-series methods. However, this orthogonalization discards magnitude information, rendering training sensitive to step-size hyperparameters and vulnerable to high-energy bursts. To mitigate this, we introduce TrasMuon (**T**rust **R**egion **A**daptive **S**caling **Muon**). TrasMuon preserves the near-isometric geometry of Muon while stabilizing magnitudes through (i) global RMS calibration and (ii) energy-based trust-region clipping. We demonstrate that while reintroducing adaptive scaling improves optimization efficiency, it typically exacerbates instability due to high-energy outliers. TrasMuon addresses this by defining a trust region based on relative energy ratios, confining updates to a stable zone. Empirical experiments on vision and language models demonstrate that TrasMuon converges faster than baselines. Furthermore, experiments without warmup stages confirm TrasMuon's superior stability and robustness.

1. Introduction

Optimizer choice remains a major bottleneck for training modern foundation models, affecting convergence speed, stability, and overall compute cost at scale (DeepSeek-AI et al., 2025; OpenAI, 2026; Anthropic, 2026). Despite substantial progress in large-scale training recipes, practitioners still face highly heterogeneous gradient landscapes and heavy-tailed/outlier updates that can trigger loss spikes and narrow the stable learning-rate region (Behrouz et al., 2025; Kimi Team et al., 2025; Park et al., 2025). A dominant baseline family is diagonal adaptivity, including Adam and its variants (Kingma & Ba, 2017; Loshchilov & Hutter, 2019; Pagliardini et al., 2025; Marfinetz, 2025), which provides robust coordinate-wise magnitude control but does not explicitly leverage matrix-level update structure.

Recent work on momentum orthogonalization has revived interest in matrix-structured updates for Transformers (Bernstein, 2025; Jordan et al., 2024). Muon-style optimizers reshape update directions via finite-step Newton–Schulz (NS) iterations toward a near-isometric factor, encouraging global feature mixing and reducing spectral anisotropy (Large et al., 2024; Bernstein & Newhouse, 2024; 2025). However, Muon-style orthogonalization predominantly constrains *geometry* (directional structure), while *effective step magnitudes* remain sensitive to calibration and training phase. Moreover, real training signals are often heavy-tailed and feature-localized: transient bursts can concentrate energy on a small subset of feature axes, leading to loss spikes and a narrow stability window if magnitudes are not carefully controlled (Behrouz et al., 2025; Kimi Team et al., 2025; Park et al., 2025).

Why adaptive scaling? In practice, a single global learning rate can correspond to markedly different parameter-space update norms across layers, tensor shapes, and early-vs-late training regimes. While near-isometric mixing can improve optimization efficiency, the lack of explicit magnitude calibration increases reliance on warmup length and schedule tuning. This motivates a lightweight, global RMS calibration to make step sizes more comparable in parameter space and to widen the usable learning-rate region.

Why a trust region on top of scaling? Global RMS calibration controls overall step magnitude but does not directly constrain *energy concentration* across feature axes. Under heavy-tailed, feature-localized bursts, a small number of columns can transiently dominate the update; in this regime, naïvely magnitude-corrected steps may still translate burst concentration into loss spikes. We therefore impose a *relative-energy trust region* that enforces a stable bound on per-feature energy ratios, e.g., $E_j/E_{\mathrm{ref}} \le \tau$, where E_j denotes column energy and E_{ref} is a robust reference. This is implemented by a multiplicative damping

[1]Huawei Canadian Research Institute, Canada [2]Department of Combinatorics and Optimization, University of Waterloo, Waterloo, Canada. Correspondence to: Peng Cheng <peng.cheng.hit@gmail.com>.

Preprint. February 17, 2026.

$c_t \in [c_{\min}, 1]^{d_{\text{in}}}$ that selectively suppresses bursty feature axes, while largely preserving the Muon-style structured mixing factor.

Our approach. We propose **TrasMuon** (**T**rust-**R**egion **A**daptive **S**caling for **Muon**), which factorizes matrix updates into a structured mixing factor and lightweight magnitude controls through multiplicative coupling. For a matrix parameter $W \in \mathbb{R}^{d_{\text{out}} \times d_{\text{in}}}$, TrasMuon applies

$$\Delta W_t \;=\; -\,\hat{\eta}_t\, O_t^{\text{base}}\, \text{diag}(c_t), \qquad c_t \in [c_{\min}, 1]^{d_{\text{in}}}. \quad (1)$$

Here O_t^{base} is a Muon-style near-isometric update factor obtained by NS orthogonalization, combined with lightweight row-wise second-moment scaling (NorMuon-style) (Li et al., 2025). Magnitude is controlled in two complementary ways: (i) an RMS-calibrated step size $\hat{\eta}_t$ that reduces step-size sensitivity and improves cross-layer calibration (Bernstein & Newhouse, 2025; Large et al., 2024); and (ii) a feature-wise trust-region damping c_t computed from relative column-energy ratios, which selectively suppresses bursty feature axes while largely preserving the structured mixing factor. To reduce dependence on schedule design and warmup length, we stabilize the damping signal over time using effective-time weighting, with weights tied to the effective step size (schedule-free style averaging) (Defazio et al., 2024).

Contributions:

- **Algorithm.** We introduce TRASMUON, combining Muon-style near-isometric mixing with global RMS calibration and a relative-energy trust region for feature-localized bursts, plus temporally stabilized damping via effective-time weighting.
- **Foundation-model training evidence.** TRASMUON improves early-stage convergence and stability in both warmup-enabled and warmup-free settings, indicating reduced step-size and schedule sensitivity.
- **Robustness.** TRASMUON consistently reduces loss spikes and yields stronger or more reliable final performance than relevant baselines under heavy-tailed and structured non-stationarity.

Implication for large-scale training. By making matrix-structured (Muon-family) updates compatible with predictable step magnitudes and outlier-resilient dynamics, TRASMUON not only converges faster than vanilla Muon, but also more stable compared to other optimizers with adaptive optimizers, with reduced reliance on delicate warmup/schedule tuning. These make TrasMuon optimizers closer to a practical, drop-in option for large-model pretraining at scale under heavy-tailed training noise.

2. Related Work

Diagonal preconditioning and Adam-style optimizers. Adaptive methods based on inexpensive diagonal second-moment estimates, most notably Adam and AdamW (Kingma & Ba, 2017; Loshchilov & Hutter, 2019), are widely used due to their robustness across architectures and training regimes. A large body of work refines Adam-style magnitude control via improved moment estimators, decay rules, or mixing strategies, aiming to better match curvature surrogates and gradient-noise statistics while retaining efficiency (Yuan et al., 2025; Pagliardini et al., 2025; Marfinetz, 2025; Shao et al., 2025; Gupta & Wojtowytsch, 2025). These methods primarily operate coordinate-wise, which can stabilize training but may underutilize matrix-level structure available in weight tensors (e.g., feature mixing across columns). TrasMuon is complementary: it retains structured mixing in matrix updates while introducing axis-selective magnitude control, rather than reverting to fully diagonal update geometry.

Matrix and block-structured preconditioning beyond diagonal adaptivity. Beyond diagonal adaptivity, classical work explores richer (block-structured) preconditioning to better capture curvature while remaining computationally feasible, including Kronecker-factored curvature approximations such as K-FAC (Martens & Grosse, 2015) and tensor/matrix second-moment preconditioners such as Shampoo (Gupta et al., 2018). Related low-memory approaches (e.g., Adafactor) exploit factored second-moment structure for large models (Shazeer & Stern, 2018). Another practical line controls step magnitudes via layerwise norm or trust-ratio scaling, comparing parameter and update norms as in LARS/LAMB (You et al., 2017; 2020). TrasMuon differs in that it does not estimate curvature factors; instead it constructs a near-isometric mixing factor via Newton–Schulz orthogonalization and stabilizes magnitudes using global RMS calibration together with a relative-energy constraint on feature axes.

Orthogonalization-based directions and Muon-style updates. Recent work revisits non-diagonal update geometry for matrix parameters using finite-step Newton–Schulz iterations to approximate polar factors of momentum updates, producing near-orthogonal (near-isometric) directions that can improve training on modern Transformer architectures (Jordan et al., 2024; Bernstein, 2025). Broader perspectives connect orthogonalized updates to modular optimization and manifold-inspired parameterizations, including variants that incorporate normalization, duality, or layer-wise geometry constraints (Bernstein & Newhouse, 2025; Large et al., 2024). A growing set of Muon-inspired variants further explores practical refinements to orthogonalized updates and their training behavior (e.g., (Pethick et al., 2025;

Ahn et al., 2025; Kumar et al., 2025; Khaled et al., 2025; Riabinin et al., 2025; Li et al., 2025)). TrasMuon builds on this line by explicitly factorizing direction construction and magnitude stabilization: it preserves a Muon-style structured mixing factor while targeting a distinct failure mode—bursty, axis-localized energy spikes—via relative-energy damping and temporal smoothing.

Trust-region magnitude control, clipping, and effective-time averaging. Magnitude control is a long-standing stability tool, ranging from global gradient clipping and its variants (Pascanu et al., 2013; Brock et al., 2021; Allouah et al., 2025) to trust-region methods that constrain per-step change (Conn et al., 2000). In large-scale training, related magnitude-control heuristics also include trust-ratio normalization (e.g., LARS/LAMB) (You et al., 2017; 2020) and classical adaptive scaling approaches such as AdaGrad (Duchi et al., 2011). Such mechanisms are often global and do not identify which feature axes dominate instability. In contrast, TrasMuon applies *feature-wise* damping based on a *relative-energy* constraint (e.g., $E_j/E_{\text{ref}} \le \tau$), selectively suppressing bursty columns while largely preserving structured mixing; global RMS calibration further improves cross-layer step-size comparability (Bernstein & Newhouse, 2025; Large et al., 2024). Finally, schedule-free and effective-time weighted averaging smooth training dynamics and reduce sensitivity to warmup length and training horizon (Defazio et al., 2024), closely related to classical Polyak–Ruppert averaging (Polyak & Juditsky, 1992; Ruppert, 1988) and multi-timescale averaging mechanisms such as SWA and Lookahead (Izmailov et al., 2018; Zhang et al., 2019). TrasMuon adopts effective-time weighted smoothing to stabilize feature-wise energy statistics under nonstationary bursts.

3. Methodology

3.1. TrasMuon Algorithm

We propose **TrasMuon** (**T**rust-**R**egion **A**daptive **S**caling for **Muon**), which *factorizes* matrix updates into a structured mixing factor and lightweight magnitude controls (global RMS calibration and feature-wise damping), as summarized in Alg. 1.

For a matrix parameter $W \in \mathbb{R}^{d_{\text{out}} \times d_{\text{in}}}$ with gradient $G_t = \nabla_W \mathcal{L}(W_t)$, TrasMuon applies the multiplicative update

$$\Delta W_t \;=\; -\,\hat{\eta}_t\, O_t^{\text{base}}\, \text{diag}(c_t), \tag{2}$$

where O_t^{base} is a structured Muon-style direction, $\hat{\eta}_t$ is an RMS-calibrated step size, and $c_t \in [c_{\min}, 1]^{d_{\text{in}}}$ is a damping-only feature (column-wise) clip.

Orthogonalized direction. We maintain momentum

$$M_t = \beta_1 M_{t-1} + (1-\beta_1) G_t, \tag{3}$$

Algorithm 1 TRASMUON: Muon + Adaptive Scaling + Trust Region + Schedule-Free Smoothed

Input: $W \in \mathbb{R}^{d_{\text{out}} \times d_{\text{in}}}$, base lr η, β_1, β_2, ϵ, NS steps T, weight decay λ, $c_{\min}$, α, β_E, β_c, trigger k, update period K, warmup T_w, mix ρ
Initialize $M \leftarrow 0$, $v^{\text{row}} \leftarrow 0$, $E^{\text{ref}} \leftarrow 0$, $c^{\text{ema}} \leftarrow \mathbf{1}$, $c^{\text{last}} \leftarrow \mathbf{1}$, $S \leftarrow 0$, $C \leftarrow \mathbf{0}$, $\gamma_t \leftarrow \eta$
repeat
  $G \leftarrow \nabla_W \mathcal{L}(W)$; $W \leftarrow (1-\eta\lambda)W$
  Momentum: $M \leftarrow \beta_1 M + (1-\beta_1)G$
  Orthogonalized direction: $O \leftarrow \text{NS}(\tilde{M}; T)$
  $v^{\text{row}} \leftarrow \beta_2 v^{\text{row}} + (1-\beta_2)\,\text{mean}_j(O_{\cdot j}^2)$
  $O^{\text{base}} \leftarrow \text{diag}\big((v^{\text{row}}+\epsilon)^{-1/2}\big)\, O$
  Calibration: $\hat{\eta} \leftarrow \eta\, \frac{\sqrt{d_{\text{out}} d_{\text{in}}}}{\|O^{\text{base}}\|_F + \epsilon}$
  Column energy: $E_j \leftarrow \sum_i M_{ij}^2$
  Robust reference: $E^{\text{cur}} \leftarrow \text{Quantile}_{0.5}(\{E_j\})$
  EMA smooth: $E^{\text{ref}} \leftarrow \beta_E E^{\text{ref}} + (1-\beta_E) E^{\text{cur}}$
  Schedule-free accumulators: $S \leftarrow S + \gamma_t^2$, $C \leftarrow C + \gamma_t^2 c^{\text{last}}$, $c^{\text{avg}} \leftarrow C/(S+\epsilon)$
  if $t > T_w$ **and** $t \bmod K = 0$ **then**
    $r_j \leftarrow E_j/(E^{\text{ref}}+\epsilon)$
    $c_j^{\text{clip}} \leftarrow \text{clip}\Big(\frac{1}{1+\alpha\log(1+r_j)},\, c_{\min},\, 1\Big)$
    Trigger (optional): $c_j^{\text{inst}} \leftarrow c_j^{\text{clip}}$ if $r_j > k$ else 1
    EMA smooth: $c^{\text{ema}} \leftarrow \beta_c c^{\text{ema}} + (1-\beta_c) c^{\text{inst}}$
  end if
  Long-Short term Mixing: $c \leftarrow \mathbf{1}$ if $t \le T_w$ else $(1-\rho)c^{\text{ema}} + \rho c^{\text{avg}}$
  $c^{\text{last}} \leftarrow c$ {cached between updates}
  Update: $W \leftarrow W - \hat{\eta}\,(O^{\text{base}} \odot \text{ExpandCols}(c))$
until training ends

remove scale via RMS pre-normalization

$$\tilde{M}_t \;=\; \frac{M_t}{\|M_t\|_F/\sqrt{d_{\text{out}} d_{\text{in}}} + \epsilon}, \tag{4}$$

and approximate the polar factor by T Newton-Schulz steps,

$$O_t \;\approx\; \text{NS}(\tilde{M}_t; T), \tag{5}$$

yielding a near-isometric direction robust to axis rotations.

Row-wise scaling calibration. We apply lightweight row-wise second-moment scaling (NorMuon-style (Li et al., 2025))

$$v_t^{\text{row}} = \beta_2 v_{t-1}^{\text{row}} + (1-\beta_2)\,\text{mean}_j(O_{t,\cdot j}^{\odot 2}), \tag{6}$$

$$O_t^{\text{base}} = \text{diag}\big((v_t^{\text{row}}+\epsilon)^{-1/2}\big)\, O_t. \tag{7}$$

We also calibrate the global step size by,

$$\hat{\eta}_t \;=\; \eta \cdot \frac{\sqrt{d_{\text{out}} d_{\text{in}}}}{\|O_t^{\text{base}}\|_F + \epsilon}, \tag{8}$$

which bounds the update RMS as $\|\Delta W_t\|_F/\sqrt{mn} \le \eta$ (since $c_t \le \mathbf{1}$), reducing sensitivity to layer shape and transient fluctuations (Bernstein & Newhouse, 2025; Large et al., 2024). Row-wise scaling serves as lightweight local conditioning, while global RMS calibration and trust-region damping provide the primary magnitude stabilization.

Trust-region clipping. This implements a relative-energy trust region by controlling the per-column ratio $r_{t,j} = E_{t,j}/(E_t^{\text{ref}} + \epsilon)$, ensuring burst-dominated columns receive multiplicative damping. In particular, damping enforces an implicit constraint of the form $r_{t,j} \lesssim \tau$ in the effective update, for a tunable tolerance controlled by α (and optional trigger k).

We measure column energies on the pre-orthogonalization momentum M_t to detect feature-localized bursts before NS mixing compresses global magnitudes and redistributes energy across axes.

$$E_{t,j} = \sum_{i=1}^{d_{\text{out}}} M_{t,ij}^2, \tag{9}$$

$$E_t^{\text{cur}} = \text{Quantile}_{0.5}(\{E_{t,j}\}), \tag{10}$$

$$E_t^{\text{ref}} = \beta_E E_{t-1}^{\text{ref}} + (1-\beta_E) E_t^{\text{cur}}, \tag{11}$$

and form $r_{t,j} = E_{t,j}/(E_t^{\text{ref}} + \epsilon)$. Using the median yields a high-breakdown reference, preventing sparse bursts from arbitrarily inflating E_t^{ref} (Hampel et al., 1986; Huber, 1981). We then apply a smooth, damping-only clip

$$c_{t,j}^{\text{raw}} = \frac{1}{1 + \alpha \log(1 + r_{t,j})}, \tag{12}$$

$$c_{t,j}^{\text{clip}} = \text{clip}\big(c_{t,j}^{\text{raw}}, c_{\min}, 1\big), \tag{13}$$

(optionally triggered only when $r_{t,j} > k$), and set c_t by temporal smoothing (more details seen in Appendix B).

Schedule-free temporal smoothing. We smooth the instantaneous clip c_t^{inst} with EMA

$$c_t^{\text{ema}} = \beta_c c_{t-1}^{\text{ema}} + (1-\beta_c) c_t^{\text{inst}}, \tag{14}$$

and optionally apply schedule-free averaging (Defazio et al., 2024) using γ_t (default $\gamma_t = \eta$):

$$S_t = S_{t-1} + \gamma_t^2, \qquad C_t = C_{t-1} + \gamma_t^2 c_{t-1}^{\text{last}}, \tag{15}$$

$$c_t^{\text{avg}} = \frac{C_t}{S_t + \epsilon}, \qquad c_t = (1-\rho) c_t^{\text{ema}} + \rho c_t^{\text{avg}}. \tag{16}$$

We cache $c_t^{\text{last}} \leftarrow c_t$ between gate updates to avoid bias when the raw clip is computed every K steps. When γ_t is constant, c_t^{avg} reduces to a long-horizon running average; when γ_t varies (e.g., due to warmup/decay), the γ_t^2 weights align the smoothing with the effective step size as in schedule-free optimization (Defazio et al., 2024).

3.2. Convergence Analysis

We briefly summarize deterministic guarantees and a standard convergence framework for TrasMuon; full statements and proofs are deferred to Appendix C. Recall $\Delta W_t = -\hat{\eta}_t U_t$ with $U_t = O_t^{\text{base}} \text{diag}(c_t)$ and $c_{t,j} \in [c_{\min}, 1]$.

Damping-only contraction. For any matrix A and any $c \in [0,1]^n$, right-multiplication by $\text{diag}(c)$ cannot increase the Frobenius norm:

$$\|A \,\text{diag}(c)\|_F \le \|A\|_F. \tag{17}$$

RMS calibration. With $\hat{\eta}_t = \eta\sqrt{mn}/(\|O_t^{\text{base}}\|_F + \epsilon)$ and damping-only $c_t \le \mathbf{1}$, the update norm is uniformly bounded:

$$\|\Delta W_t\|_F \le \eta\sqrt{mn} \qquad \forall t, \tag{18}$$

independently of transient gradient spikes.

Stationarity under smoothness and alignment. Under standard L-smoothness and a mild alignment condition (Appendix C), TrasMuon satisfies an expected first-order stationarity bound of the form

$$\frac{1}{T}\sum_{t=0}^{T-1} \mathbb{E}\|\nabla f(W_t)\|_F^2 \;\le\; \frac{\mathbb{E}[f(W_0)] - f^\star}{\mu\,\eta\,T} \;+\; \frac{L}{2\mu}\,\eta\,mn, \tag{19}$$

for a constant $\mu > 0$ capturing effective descent. Importantly, the EMA/schedule-free construction of c_t only affects how the clip is computed, while the theory relies solely on the invariant $c_{t,j} \in [c_{\min}, 1]$.

4. Experiments

4.1. Language Model Pretraining: Fast Early Descent and Late-Stage Dynamics

Language model training setup. TRASMUON is evaluated in a controlled, short-run pretraining-style setting and compared against four baseline optimizers: AdamW (Loshchilov & Hutter, 2019), Muon (Jordan et al., 2024), Dion (Ahn et al., 2025), and NorMuon (Li et al., 2025). All methods train decoder-only Transformer models from random initialization, including GPT-2 (Radford et al., 2019) and Qwen3-0.6B (Yang et al., 2025), on FineWeb-Edu (Lozhkov et al., 2024). Each run is executed for 1500 optimization steps with sequence length 1024 and a fixed global (effective) batch size of 1024 across models and optimizers, corresponding to $1500 \times 1024 \times 1024 \approx 1.57 \times 10^9$ training tokens.

Optimization hyperparameters and sensitivity. To isolate optimizer behavior under an identical training budget, all methods share the same learning rate $\eta = 3.6 \times 10^{-3}$ and weight decay $\lambda = 5 \times 10^{-3}$. All runs follow the same default seeding behavior of the training stack. For NorMuon in particular, the most influential optimizer-specific hyperparameter is the RMS normalization, which controls scale calibration of the orthogonalized update. This section is treated as a fixed-hyperparameter pilot, where broader sweeps and multi-seed evaluations are left to future work.

Learning-rate schedule and reporting. A warmup–stable–decay learning-rate schedule is adopted, and results are reported for both warmup-enabled and warmup-free configurations. All other training components, including the data pipeline, batching, tokenization, model architecture, and compute budget, are kept identical across optimizers.

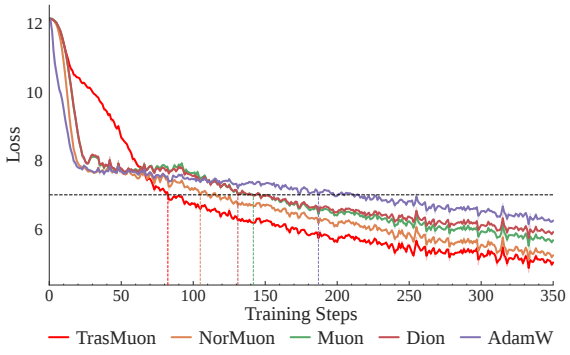

(a) Qwen3-0.6B with warmup

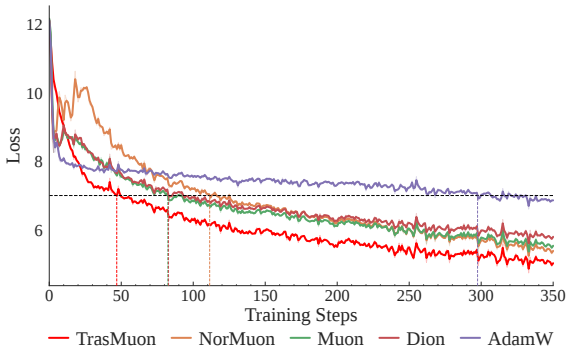

(b) Qwen3-0.6B without warmup

Figure 1. Early-stage training dynamics for Qwen3-0.6B from scratch (steps 0–350) under a warmup-stable-decay schedule, comparing (a) warmup-enabled runs and (b) warmup-free runs. The curves are smoothed using a time-weighted exponential moving average (EMA) with smoothing factor 0.1 for better visualization.

Training with warmup. Under the warmup-enabled schedule, all evaluated optimizers exhibit stable training in this fixed-hyperparameter pilot. Although TRASMUON is not the fastest within the first few dozen steps, it begins to reduce loss more rapidly after approximately 80 steps (illustrated in Fig. 1a). At a reference threshold of training loss ($= 7.0$), TRASMUON reaches the target in 80 steps, compared to 188 steps for AdamW ($2.35\times$) and 140 steps for Muon ($1.75\times$).[1]

Training without warmup. Without warmup, optimizer becomes more sensitive to step-size calibration. Under the same shared learning rate and batch/sequence configuration, TRASMUON maintains a smooth loss trajectory in the early stage, while several baselines show larger loss oscillations as shown in Fig. 1b. At the same reference threshold of training loss, TRASMUON reaches the target in 48 steps, versus 298 for AdamW ($6.21\times$) and 83 for Muon ($1.73\times$). Despite the widespread use of warmup in pretraining, this setting remains meaningful, as the choice of warmup length is typically determined heuristically.

Late-stage behavior under a fixed budget. Beyond early-stage speed, TRASMUON also attains the lowest (or comparable-lowest) training loss in the late-stage window under both warmup settings in this pilot run. Late-stage curves and loss comparisons are reported in Fig. 6 of Appendix D.1. The early-stage gap narrows as training progresses into a slower-loss regime, suggesting that the benefit is strongest when training dynamics are most nonstationary.

Decreasing feature-wise energy concentration over training. A plausible explanation is that early training exhibits stronger feature-wise anisotropy, where a small subset of hidden dimensions (columns) contributes disproportionately to gradient or momentum energy. In this regime, TRASMUON's energy-based feature-wise clipping is engaged, selectively damping bursty columns and improving stability without discarding the structured Muon direction. As representations become better calibrated, energy may become more uniformly distributed across feature axes, reducing the prevalence of strongly concentrated column-localized bursts; consequently, the clipping signal weakens and the effective update becomes closer to the NorMuon backbone. This explanation is offered as a hypothesis and a direct characterization of activation/gradient anisotropy (e.g., via tracked energy ratios and gate statistics over time) is left to future work.

4.2. Vision Transformer Experiments

ImageNet-100: Vision Transformer Training. We evaluate the benefits of TrasMuon in a large-scale vision setting by training ViT-Base (Dosovitskiy et al., 2021) on ImageNet-100 due to limited computational resources, a 100-class subset of ImageNet-1k (ILSVRC-2012) (Deng et al., 2009), followed the standard ILSVRC-2012 train/validation protocol. Dataset construction, class specification, and implementation details for ViT training are provided in Appendix E.1 and E.2. We compared AdamW, Muon, NorMuon, and TRASMUON, using identical training budgets and hyperparameters. Results show training loss and *validation* top-1 accuracy, aggregated over three random seeds.

Results. Across all optimizers evaluated with multi-seed runs, Muon, Normuon, and TRASMUON consistently improve optimization behavior and validation accuracy over

[1] We use loss $= 7.0$ as a representative checkpoint.

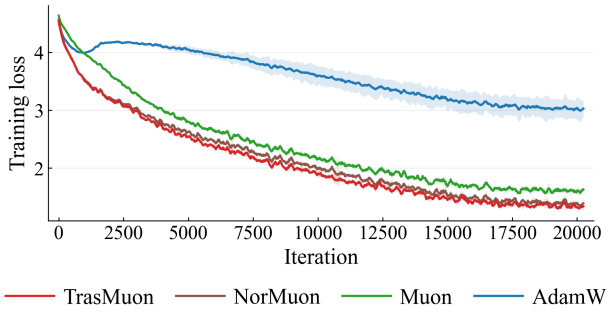

(a) Training loss vs. iteration.

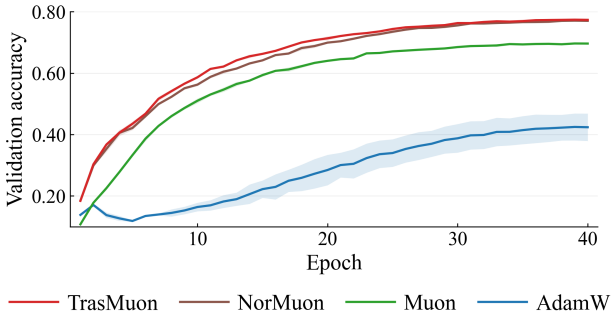

(b) Validation top-1 accuracy vs. epoch.

Figure 2. ViT-Base training on ImageNet-100. Multi-seed results (mean ± std over three seeds: 42, 43, 44) for 4 optimizers. Shaded regions denote variability across seeds.

AdamW in these experiments, demonstrating the advantage of optimizers, which update based on structured, near-orthogonal update directions. illustrated in Fig. 2a and Fig. 2b, TRASMUON achieves the fastest loss reduction, the highest validation accuracy, and reduced variability across different seeds and various compared optimizers. Moreover, CIFAR-100 has been evaluated robustness under controlled column-localized burst injection in Appendix E.3.

4.3. PINNs Benchmark: ROI Sampling as a Nonstationary Stress Test

Adaptive collocation in physics-informed neural networks (PINNs) is often necessary to resolve localized errors and stiff PDE behavior, where uniform sampling under-resolves difficult regions (Gao et al., 2023; Subramanian et al., 2022; Wu et al., 2023). Here we use region-of-interest (ROI) densification as a *controlled nonstationarity* mechanism to stress-test optimizer robustness: periodically concentrating interior collocation points in a small subregion induces distribution shifts in the residual samples, perturbing gradient statistics in a reproducible way.

Helmholtz equation setup. On $\Omega = [0,1]^2$, we consider

$$\Delta u(x) + \kappa^2 u(x) = f(x), \qquad u|_{\partial\Omega} = 0, \tag{20}$$

with the manufactured solution

$$u^\star(x,y) = \sin(\pi k x)\sin(\pi k y), \qquad \kappa = \pi k. \tag{21}$$

which yields $f(x) = -(\pi k)^2 u^\star(x)$.

We train an MLP $u_\theta : \Omega \to \mathbb{R}$ by minimizing

$$\mathcal{L}(\theta) = \mathbb{E}\left[\tfrac{1}{2} r_\theta(x)^2\right] + \lambda_b \mathbb{E}\left[\tfrac{1}{2}\big(u_\theta(x) - u^\star(x)\big)^2\right] \tag{22}$$

$$r_\theta(x) = \Delta u_\theta(x) + \kappa^2 u_\theta(x) - f(x). \tag{23}$$

and report the relative error on a fixed evaluation grid

$$\text{rel-}L_2(u_\theta, u^\star) = \frac{\|u_\theta - u^\star\|_2}{\|u^\star\|_2}. \tag{24}$$

ROI sampling protocol. To emulate adaptive densification, we use a time-varying interior sampling distribution

$$p_t(x) = (1-\alpha_t)\, p_0(x) + \alpha_t\, p_{\text{roi}}(x), \tag{25}$$

where p_0 is uniform over Ω and p_{roi} is uniform over $\Omega_{\text{roi}} = [x_0, x_1]\times[y_0, y_1]$. We run 4000 optimization steps and begin nonstationary ROI events after step 1000. At each ROI event (every 20 steps), 95% of interior points are sampled from a small ROI patch and the rest from the full domain. To avoid sensitivity to a single ROI location, the patch is drawn from a fixed pool (corners, edges, and interior patches) using a step-dependent hash for reproducibility. This produces repeated, time-varying distribution shifts that mimic practical ROI refinement policies.

PINN ROI-sampling stress test: convergence and robustness. Figure 3a and 3b compare Muon and TRASMUON on Helmholtz (k=2) under a controlled nonstationary ROI-sampling protocol, where ROI events start at step 1000 and recur every 20 steps. During the initial stationary phase (before ROI events), both methods exhibit nearly identical optimization trajectories in terms of training loss and domain-wide relative L_2 error, indicating that TRASMUON does not incur a measurable overhead or degradation under standard uniform sampling.

After ROI events begin, the training objective becomes significantly more variable due to the induced distribution shifts in interior collocation points. In this nonstationary regime, TRASMUON maintains comparable or slightly lower training loss while exhibiting reduced extreme fluctuations, consistent with its design goal of suppressing bursty, feature-localized updates. These results support the conclusion that TRASMUON preserves baseline convergence under stationary sampling, while improving stability and final solution accuracy under controlled, nonstationary ROI sampling shifts.

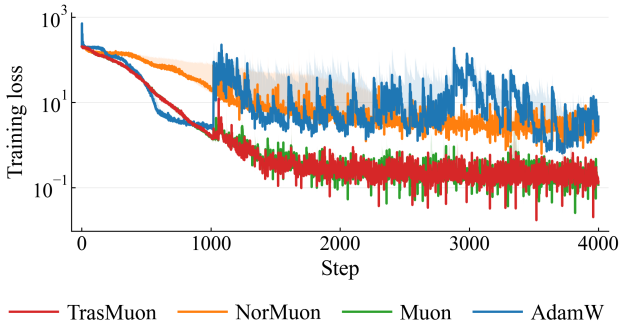

(a) training objective (estimated on the time-varying sampling distribution p_t)

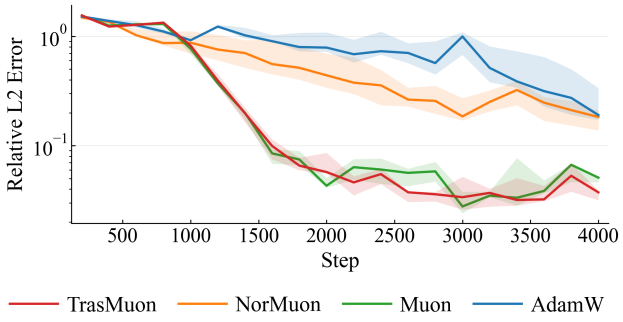

(b) domain-wide relative L_2 error evaluated on a fixed grid. ROI events start at step 1000 and repeat every 20 steps

Figure 3. **PINN Helmholtz (k=2) under random ROI sampling shifts.** Curves show the mean over seeds, and shaded regions indicate variability across seeds.

4.4. Mechanistic Study: Column-Localized Outliers and Energy-Based Feature Clipping

We design a controlled toy problem to validate the *feature-wise clipping* mechanism in TRASMUON under intermittent, column-localized bursts. We optimize a matrix parameter $W \in \mathbb{R}^{d\times d}$ under the quadratic objective

$$\min_W \; f(W) \;=\; \tfrac{1}{2}\|AWB - T\|_F^2, \tag{26}$$

where $A = U\Sigma_A U^\top$ and $B = V\Sigma_B V^\top$ with random orthogonal U, V, and diagonal spectra Σ_A, Σ_B chosen to yield a target condition number $\kappa \in \{10^2, 10^4, 10^6\}$. This construction controls stiffness while allowing us to randomize nuisance rotations across runs.

Column-localized outlier injection (stress protocol). To emulate rare, feature-localized gradient domination, every K_{out} steps we inject an outlier event that amplifies a small subset of columns in a fixed feature basis. Concretely, for momentum M_t we select a set $\mathcal{J}$ of $s \ll d$ column indices and apply a multiplicative burst

$$\widetilde{M}_{t,\cdot j} \;=\; \begin{cases} a\, M_{t,\cdot j}, & \text{if } j \in \mathcal{J}, \\ M_{t,\cdot j}, & \text{otherwise}, \end{cases} \tag{27}$$

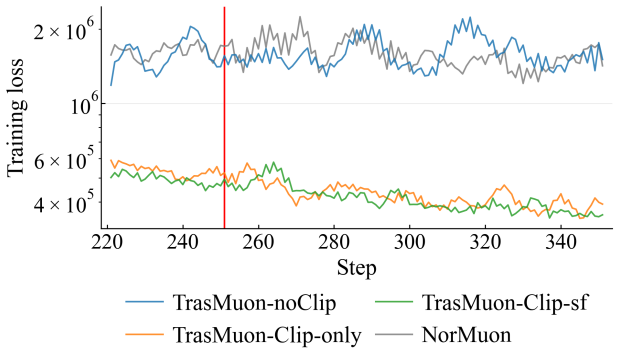

Figure 4. **Column outlier injection.** Loss trajectories in a window around an outlier event. Vertical markers indicate outlier steps.

with burst amplitude $a > 1$. This perturbation produces abrupt increases in column energy $E_{t,j} = \sum_i \widetilde{M}^2_{t,ij}$ while leaving the underlying objective (26) unchanged.

Preserving feature semantics. Because TRASMUON's clipping is axis-aligned (column-wise), the stress protocol is evaluated under a `fix_V=True` setting, i.e., the column basis is preserved across training and across injected events. We additionally report a boundary condition where the column basis is randomized (`fix_V=False`); in that case, injected energy disperses across columns and feature-wise clipping is not expected to yield an advantage (Appendix G).

Metrics. We track (i) spike count and (ii) final objective value, reporting median and IQR over multiple seeds/rotations.

Closed-loop response. Figure 4 shows that TRASMUON reduces burst-induced loss spikes and improves convergence relative to the NorMuon backbone under matched compute. Figure 5 provides mechanism-level evidence consistent with a closed-loop response: outlier events increase the relative column-energy ratio (e.g., $r_{q95}/r_{\max}$), which is immediately followed by a decrease in the *applied* clipping signal (tracked by $c_{\text{used,min}}$), thereby damping the burst and suppressing spikes.

Not a trivial step-size reduction. To rule out the confound that improvements arise from a global effective step-size change, we include a TRASMUON-NOCLIP ablation that disables feature-wise clipping while keeping all other components identical. As summarized in Table 1, TRASMUON-NOCLIP behaves similarly to NorMuon, whereas enabling clipping yields a clear reduction in spike statistics and a large improvement in the final objective, isolating the contribution of feature-wise clipping.

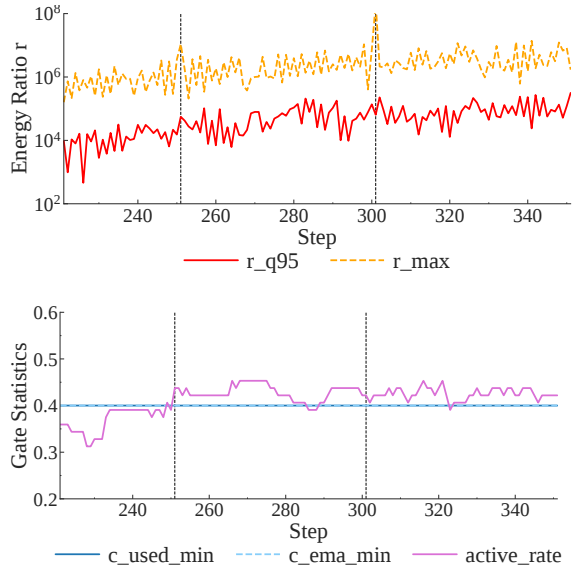

Figure 5. **Closed-loop clipping evidence.** Outlier events increase the column-energy ratio in log-scale (top), followed by stronger *feature-wise clipping* in the applied coefficients (bottom; $c_{\text{used,min}}$).

Table 1. **Mechanistic study summary under `fix_V=True`.** TRASMUON-NOCLIP removes feature-wise clipping while keeping the rest identical. We report median with IQR across runs; lower is better.

Method	Spike Count	Final Loss
NorMuon	44 (35,56)	1.3e+06 (1.0e+06,1.6e+06)
TRASMUON-noClip	48 (38,56)	1.1e+06 (8.9e+05,1.9e+06)
TRASMUON-Clip-only	**28** (24,34)	2.4e+05 (2.0e+05,2.8e+05)
TRASMUON-Clip-sf	30 (24,36)	**2.0e+05** (1.6e+05,2.7e+05)

Boundary condition (feature semantics broken). When the column basis is randomized, the advantage of feature-wise clipping diminishes (Appendix G), consistent with the intended mechanism: axis-aligned clipping requires a meaningful feature basis.

5. Discussion and Limitations

What TRASMUON changes. TRASMUON factorizes matrix updates into (i) a Muon-style near-isometric mixing factor constructed by Newton–Schulz orthogonalization and (ii) explicit magnitude controls: a global RMS-calibrated step size and a bounded, damping-only feature-wise coefficient $c_{t,j} \in [c_{\min}, 1]$. This design targets a common practical tension: structured mixing can improve optimization geometry, while stable magnitudes govern learning-rate sensitivity and robustness to heavy-tailed bursts. When feature axes are semantically meaningful and bursts are axis-localized, relative-energy damping selectively attenuates high-energy columns while largely preserving the Muon-style mixing structure.

When feature-wise damping and effective-time smoothing help. Feature-wise damping is most beneficial when update energy concentrates on a small subset of feature axes, reflected by large relative ratios $r_{t,j} = E_{t,j}/(E_t^{\text{ref}} + \epsilon)$. In this regime, multiplicative damping suppresses burst-dominated columns without amplification. When clipping is recomputed sparsely (every K steps) or schedules vary, effective-time (schedule-free) averaging provides a stable long-horizon estimate by accumulating γ_t^2-weighted statistics, reducing sensitivity to recomputation frequency and schedule details.

Limitations. (i) The formulation is most natural for 2D weight matrices; extending energy diagnostics and damping to embeddings and higher-order tensors requires careful axis conventions. (ii) Newton–Schulz orthogonalization is sensitive to numerical precision; large-scale deployment benefits from precision-aware implementations. (iii) TRASMUON introduces additional hyperparameters and design choices (e.g., $K, \alpha, k, c_{\min}, \rho$ and the robust reference), and their interactions with model scale and data regimes merit broader sweeps.

6. Conclusion

We presented TRASMUON, a Muon-family optimizer that combines (i) NS-based near-isometric mixing factors with (ii) explicit magnitude stabilization via global RMS calibration and bounded, damping-only feature-wise clipping, optionally smoothed by effective-time (schedule-free) averaging. Across the evaluated workloads, TRASMUON improves training stability and achieves competitive or better final performance than strong baselines. Controlled diagnostics further support the intended mechanism: column-localized energy bursts increase relative energy ratios and lead to stronger applied damping, while ablations (e.g., NOCLIP) and broken-axis settings help rule out trivial explanations such as uniform step-size reduction. On practical tasks including language-model training, vision transformers, and PINNs under ROI-induced sampling shifts, TRASMUON yields faster or more stable optimization dynamics and improved robustness.

Several extensions remain. Feature-wise damping is currently formulated for 2D matrices; extending it to embeddings and higher-order tensors requires principled axis conventions and efficient implementations. NS orthogonalization adds compute and can be sensitive to numerical precision, motivating precision-aware and mixed-precision robust variants. Finally, a fuller theory connecting orthogonalized mixing, axis-selective damping, and generalization remains open (Appendix A).

Impact Statement

This paper presents work whose goal is to advance the field of machine learning. There are many potential societal consequences of our work, none of which we feel must be specifically highlighted here.

References

Ahn, K., Xu, B., Abreu, N., Fan, Y., Magakyan, G., Sharma, P., Zhan, Z., and Langford, J. Dion: Distributed orthonormalized updates. *arXiv preprint arXiv:2504.05295*, 2025.

Allouah, Y., Guerraoui, R., Gupta, N., Jellouli, A., Rizk, G., and Stephan, J. Adaptive gradient clipping for robust federated learning. In *International Conference on Learning Representations*, 2025.

Ambityga. ImageNet100. https://www.kaggle.com/datasets/ambityga/imagenet100, 2021. Accessed: 2026-01-23.

Anthropic. Introducing Claude Opus 4.5, 2026. URL https://www.anthropic.com/news/claude-opus-4-5. Accessed: 2026-01-12.

Behrouz, A., Li, Z., Kacham, P., Daliri, M., Deng, Y., Zhong, P., Razaviyayn, M., and Mirrokni, V. ATLAS: Learning to optimally memorize the context at test time. *arXiv preprint arXiv:2505.23735*, 2025.

Bernstein, J. Deriving Muon, 2025. URL https://jeremybernste.in/writing/deriving-muon.

Bernstein, J. and Newhouse, L. Old optimizer, new norm: An anthology. In *OPT 2024: Optimization for Machine Learning*, 2024.

Bernstein, J. and Newhouse, L. Modular duality in deep learning. In *International Conference on Machine Learning*, 2025.

Brock, A., De, S., Smith, S. L., and Simonyan, K. High-performance large-scale image recognition without normalization. In *International Conference on Machine Learning*, 2021.

Conn, A. R., Gould, N. I. M., and Toint, P. L. *Trust Region Methods*. SIAM, 2000.

DeepSeek-AI, Liu, A., Feng, B., Xue, B., Wang, B., et al. DeepSeek-V3 technical report. *arXiv preprint arXiv:2412.19437*, 2025.

Defazio, A., Yang, X. A., Khaled, A., Mishchenko, K., Mehta, H., and Cutkosky, A. The road less scheduled. In *Advances in Neural Information Processing Systems*, 2024.

Deng, J., Dong, W., Socher, R., Li, L.-J., Li, K., and Fei-Fei, L. Imagenet: A large-scale hierarchical image database. In *IEEE Conference on Computer Vision and Pattern Recognition*, 2009.

Dosovitskiy, A., Beyer, L., Kolesnikov, A., Weissenborn, D., Zhai, X., Unterthiner, T., Dehghani, M., Minderer, M., Heigold, G., Gelly, S., Uszkoreit, J., and Houlsby, N. An image is worth 16x16 words: Transformers for image recognition at scale. In *International Conference on Learning Representations*, 2021.

Duchi, J., Hazan, E., and Singer, Y. Adaptive subgradient methods for online learning and stochastic optimization. *Journal of Machine Learning Research*, 12:2121–2159, 2011.

Gao, Z., Yan, L., and Zhou, T. Failure-informed adaptive sampling for PINNs. *SIAM Journal on Scientific Computing*, 45(4):A1971–A1994, 2023.

Gupta, K. and Wojtowytsch, S. Nesterov acceleration in benignly non-convex landscapes. In *The International Conference on Learning Representations*, 2025.

Gupta, V., Koren, T., and Singer, Y. Shampoo: Preconditioned stochastic tensor optimization. In *International Conference on Machine Learning*, 2018.

Hampel, F. R., Ronchetti, E. M., Rousseeuw, P. J., and Stahel, W. A. *Robust Statistics: The Approach Based on Influence Functions*. John Wiley & Sons, 1986.

Huber, P. J. *Robust Statistics*. John Wiley & Sons, 1981.

Izmailov, P., Wilson, A., Podoprikhin, D., Vetrov, D., and Garipov, T. Averaging weights leads to wider optima and better generalization. In *Conference on Uncertainty in Artificial Intelligence*, 2018.

Jordan, K., Jin, Y., Boza, V., You, J., Cesista, F., Newhouse, L., and Bernstein, J. Muon: An optimizer for hidden layers in neural networks, 2024. URL https://kellerjordan.github.io/posts/muon/.

Khaled, A., Ozkara, K., Yu, T., Hong, M., and Park, Y. MuonBP: Faster Muon via block-periodic orthogonalization. *arXiv preprint arXiv:2510.16981*, 2025.

Kimi Team, Bai, Y., Bao, Y., Chen, G., Chen, J., Chen, N., Chen, R., et al. Kimi K2: Open agentic intelligence. *arXiv preprint arXiv:2507.20534*, 2025.

Kingma, D. P. and Ba, J. Adam: A method for stochastic optimization. *arXiv preprint arXiv:1412.6980*, 2017.

Kumar, B., Jin, R., and Quesnelle, J. CurvaDion: Curvature-adaptive distributed orthonormalization. *arXiv preprint arXiv:2512.13728*, 2025.

Large, T., Liu, Y., Huh, M., Bahng, H., Isola, P., and Bernstein, J. Scalable optimization in the modular norm. In *Advances in Neural Information Processing Systems*, 2024.

Li, Z., Liu, L., Liang, C., Chen, W., and Zhao, T. NorMuon: Making Muon more efficient and scalable. *arXiv preprint arXiv:2510.05491*, 2025.

Loshchilov, I. and Hutter, F. Decoupled weight decay regularization. In *International Conference on Learning Representations*, 2019.

Lozhkov, A., Ben Allal, L., von Werra, L., and Wolf, T. FineWeb-Edu: The finest collection of educational content, 2024. URL https://huggingface.co/datasets/HuggingFaceFW/fineweb-edu. Accessed: 2026-01-01.

Marfinetz, M. Evolving Deep Learning Optimizers. *arXiv preprint arXiv:2512.11853*, 2025.

Martens, J. and Grosse, R. Optimizing neural networks with kronecker-factored approximate curvature. In *International Conference on Machine Learning*, 2015.

OpenAI. Introducing GPT-5.2, 2026. URL https://openai.com/index/introducing-gpt-5-2/. Accessed: 2026-01-12.

Pagliardini, M., Ablin, P., and Grangier, D. The AdEMAMix optimizer: Better, faster, older. In *International Conference on Learning Representations*, 2025.

Park, J., Lee, T., Yoon, C., Hwang, H., and Kang, J. Outlier-safe pre-training for robust 4-Bit quantization of large language models. *arXiv preprint arXiv:2506.19697*, 2025.

Pascanu, R., Mikolov, T., and Bengio, Y. On the difficulty of training recurrent neural networks. In *International Conference on Machine Learning*, 2013.

Pethick, T., Xie, W., Antonakopoulos, K., Zhu, Z., Silveti-Falls, A., and Cevher, V. Training deep learning models with norm-constrained LMOs. In *International Conference on Machine Learning*, 2025.

Polyak, B. T. and Juditsky, A. B. Acceleration of stochastic approximation by averaging. *SIAM Journal on Control and Optimization*, 1992.

Radford, A., Wu, J., Child, R., Luan, D., Amodei, D., Sutskever, I., et al. Language models are unsupervised multitask learners. *OpenAI blog*, 2019.

Riabinin, A., Shulgin, E., Gruntkowska, K., and Richtárik, P. Gluon: Making Muon & Scion great again! (bridging theory and practice of LMO-based optimizers for LLMs). *arXiv preprint arXiv:2505.13416*, 2025.

Ruppert, D. Efficient estimations from a slowly convergent robbins–monro process. Technical report, Cornell University, ORIE, 1988.

Shao, Y., Weng, S., Sun, H., Gao, Q., Zhang, L., Mao, Z., Xu, S., Zhang, Z., and Xing, L. BDS-Adam optimizer integrating adaptive variance rectification with semi-adaptive gradient smoothing. *Scientific Reports*, 15 (1):36906, 2025.

Shazeer, N. and Stern, M. Adafactor: Adaptive learning rates with sublinear memory cost. In *International Conference on Machine Learning*, 2018.

Subramanian, S., Kirby, R. M., Mahoney, M. W., and Gholami, A. Adaptive self-supervision algorithms for physics-informed neural networks. *arXiv preprint arXiv:2207.04084*, 2022.

Touvron, H., Cord, M., Douze, M., Massa, F., Sablayrolles, A., and Jégou, H. Training data-efficient image transformers & distillation through attention. In *International Conference on Machine Learning*, 2021.

Wu, C., Zhu, M., Tan, Q., Kartha, Y., and Lu, L. A comprehensive study of non-adaptive and residual-based adaptive sampling for physics-informed neural networks. *Computer Methods in Applied Mechanics and Engineering*, 403:115671, 2023.

Yang, A., Li, A., Yang, B., Zhang, B., Hui, B., Zheng, B., Yu, B., Gao, C., Huang, C., Lv, C., et al. Qwen3 technical report. *arXiv preprint arXiv:2505.09388*, 2025.

You, Y., Gitman, I., and Ginsburg, B. Large batch training of convolutional networks. *arXiv preprint arXiv:1708.03888*, 2017.

You, Y., Li, J., Reddi, S., Hseu, J., Kumar, S., Bhojanapalli, S., Song, X., Demmel, J., Keutzer, K., and Hsieh, C.-J. Large batch optimization for deep learning: Training bert in 76 minutes. In *International Conference on Learning Representations*, 2020.

Yuan, H., Liu, Y., Wu, S., Zhou, X., and Gu, Q. MARS: Unleashing the power of variance reduction for training large models. In *International Conference on Machine Learning*, 2025.

Zhang, M., Lucas, J., Ba, J., and Hinton, G. E. Lookahead optimizer: k steps forward, 1 step back. *Advances in Neural Information Processing Systems*, 2019.

A. Future Work

- **Theory and guarantees.** Develop stability and convergence analyses for orthogonalized updates combined with bounded, damping-only feature-wise clipping. A promising direction is to formalize a Lyapunov-style descent argument under explicit alignment conditions and bounded-update properties, and to connect empirical spectral diagnostics (e.g., the effective update statistic $A_{\text{eff}} = W^\top \Delta W$) to provable stability regimes.
- **Generalizing feature axes beyond 2D matrices.** Extend EnergyCol-style clipping to convolutional kernels, embeddings, and higher-order tensors by defining principled "feature axes" (e.g., input-channel, attention-head, or group dimensions). We also plan to explore block-wise and low-rank variants that preserve interpretability while reducing per-step overhead.
- **Adaptive burst modeling with transparent control.** Replace fixed clipping hyperparameters (e.g., $c_{\min}$, α, update period K) with lightweight, interpretable adaptations driven by online tail statistics of the energy distribution (quantiles, kurtosis, robust outlier scores), while maintaining the damping-only constraint and avoiding hidden amplification.
- **Systems and numerical precision.** Improve the efficiency and robustness of Newton–Schulz orthogonalization in mixed precision and distributed settings. This includes precision-aware kernels, communication-efficient implementations, and amortized/approximate orthogonalization strategies that retain most of the directional benefit at lower cost.
- **Broader robustness regimes and downstream impact.** Evaluate TRASMUON under realistic forms of nonstationarity common in large-scale training (curriculum shifts, domain-mixture changes, sequence-length spikes, and data-quality transitions), and study how clipping statistics correlate with downstream robustness and generalization.

B. TrasMuon Algorithm (Extended)

We present **TrasMuon** (**T**rust **R**egion **A**daptive **S**caling for **Muon**), which explicitly decouples *update geometry* (direction) from *step-size control* (magnitude). For a matrix parameter $W \in \mathbb{R}^{d_{\text{out}} \times d_{\text{in}}}$ with stochastic gradient $G_t = \nabla_W \mathcal{L}(W_t)$, TrasMuon applies multiplicative coupling

$$\Delta W_t \;=\; -\,\hat{\eta}_t\, O_t^{\text{base}}\, \text{diag}(c_t), \tag{28}$$

where $O_t^{\text{base}} \in \mathbb{R}^{d_{\text{out}} \times d_{\text{in}}}$ provides a structured direction, $\hat{\eta}_t$ is a row-wise RMS-calibrated global step size, and $c_t \in [c_{\min}, 1]^{d_{\text{in}}}$ is a *feature-axis* (column-wise) damping vector (damping-only, no amplification).

B.1. Orthogonalized Directions via Newton–Schulz

TrasMuon maintains an exponential moving average of gradients

$$M_t \;=\; \beta_1 M_{t-1} + (1-\beta_1) G_t. \tag{29}$$

To extract a rotation-robust, near-isometric direction, we approximate the polar factor of M_t. For numerical stability of Newton–Schulz (NS) iterations, we remove the scale gauge by RMS-normalizing

$$\tilde{M}_t \;=\; \frac{M_t}{\|M_t\|_F / \sqrt{d_{\text{out}} d_{\text{in}}} + \epsilon}, \tag{30}$$

and apply T NS steps to obtain

$$O_t \;\approx\; \text{NS}(\tilde{M}_t; T) \;\approx\; \tilde{M}_t (\tilde{M}_t^\top \tilde{M}_t)^{-1/2}, \tag{31}$$

yielding a structured direction that is less sensitive to axis rotations than elementwise or diagonal preconditioning (e.g., Muon-style orthogonalized updates).

B.2. Row-Second-Moment Scaling and RMS-Calibrated Step Size

Orthogonalization primarily shapes *direction*. To stabilize *magnitude* across layers and time, we apply lightweight row-wise second-moment scaling (as in NorMuon (Li et al., 2025)):

$$v_t^{\text{row}} \;=\; \beta_2 v_{t-1}^{\text{row}} + (1-\beta_2)\, \text{mean}_j \left(O_{t,\cdot j}^{\odot 2} \right), \tag{32}$$

$$O_t^{\text{base}} \;=\; \operatorname{diag}\big((v_t^{\text{row}} + \epsilon)^{-1/2}\big)\, O_t. \tag{33}$$

Row scaling addresses row-wise heterogeneity, while a *global* row-wise calibration controls the update norm. We set

$$\hat{\eta}_t \;=\; \eta \cdot \frac{\sqrt{d_{\text{out}} d_{\text{in}}}}{\|O_t^{\text{base}}\|_F + \epsilon}, \tag{34}$$

so that the per-step RMS magnitude of ΔW_t is on the order of η. Since $c_t \le \mathbf{1}$ elementwise, (34) also implies an explicit Frobenius-norm bound $\|\Delta W_t\|_F \le \eta\sqrt{d_{\text{out}} d_{\text{in}}}$ (up to ϵ), reducing sensitivity to layer shape and fluctuations in the orthogonalized direction (Bernstein & Newhouse, 2025; Large et al., 2024).

B.3. Energy-Based Feature Clipping

Motivation. In practice, instability often arises from *bursty magnitudes* that concentrate on a small subset of feature axes (columns), causing loss spikes and narrowing the stable learning-rate region. TrasMuon therefore introduces *feature-wise clipping*: it dampens only the high-energy feature directions while preserving the Muon-like direction structure in O_t^{base}.

Column energy and a robust reference. We measure column energy from momentum M_t:

$$E_{t,j} \;=\; \sum_{i=1}^{d_{\text{out}}} M_{t,ij}^2, \qquad j = 1, \dots, d_{\text{in}}. \tag{35}$$

We summarize the typical energy level at step t by a quantile statistic

$$E_t^{\text{cur}} \;=\; \text{Quantile}_q\big(\{E_{t,j}\}_{j=1}^{d_{\text{in}}}\big), \qquad q = 0.5, \tag{36}$$

and maintain a running reference via an EMA updated every step:

$$E_t^{\text{ref}} \;=\; \beta_E E_{t-1}^{\text{ref}} + (1 - \beta_E)\, E_t^{\text{cur}}. \tag{37}$$

Using a quantile (median) yields a high-breakdown reference: the sample median has a 50% breakdown point, so a sparse set of high-energy columns cannot arbitrarily inflate E_t^{ref} and thereby "move the clipping threshold" in response to the outliers being clipped (Hampel et al., 1986; Huber, 1981).

Relative ratio and clipping-style damping. We form a dimensionless ratio

$$r_{t,j} \;=\; \frac{E_{t,j}}{E_t^{\text{ref}} + \epsilon}. \tag{38}$$

A hard energy cap $E_{t,j} \le k\, E_t^{\text{ref}}$ gives the column-wise analogue of norm clipping:

$$c_{t,j}^{\text{hard}} \;=\; \min\left(1, \sqrt{\frac{k\, E_t^{\text{ref}}}{E_{t,j} + \epsilon}}\right), \tag{39}$$

which enforces $r_{t,j} \le k$ after rescaling. In TrasMuon we use a smooth, numerically stable *soft clipping* rule:

$$c_{t,j}^{\text{raw}} \;=\; \frac{1}{1 + \alpha \log(1 + r_{t,j})}, \qquad c_{t,j}^{\text{gate}} \;=\; \text{clip}\big(c_{t,j}^{\text{raw}},\, c_{\min},\, 1\big)\,. \tag{40}$$

This rule is bounded and avoids power-law instabilities as $r_{t,j} \to 0$. Importantly, $c_{t,j} \le 1$ for all j, so the mechanism is strictly damping-only and can be interpreted as a trust-region safety mechanism in *feature space*.

Triggered vs. continuous clipping. Optionally, we apply damping only when $r_{t,j}$ exceeds a trigger k:

$$\bar{c}_{t,j} \;=\; \begin{cases} c_{t,j}^{\text{gate}}, & r_{t,j} > k, \\ 1, & \text{otherwise}, \end{cases} \tag{41}$$

so that non-burst columns remain unchanged and the gate acts as an event-driven clip.

B.4. Temporal Smoothing and Schedule-Free Averaging

To reduce short-term noise and avoid sensitivity to the gate-update period, we smooth the instantaneous clip. Let c_t^{inst} denote the clip applied at step t (either c_t^{gate} or $\bar{c}_t$ depending on triggering). We first apply EMA smoothing:

$$c_t^{\text{ema}} \;=\; \beta_c c_{t-1}^{\text{ema}} + (1-\beta_c) c_t^{\text{inst}}. \tag{42}$$

Second, we maintain a schedule-free average using an effective step weight γ_t (default $\gamma_t = \eta$) (Defazio et al., 2024). Define the scalar accumulator $S_t \in \mathbb{R}$ and vector accumulator $C_t \in \mathbb{R}^{d_{\text{in}}}$:

$$S_t \;=\; S_{t-1} + \gamma_t^2, \qquad C_t \;=\; C_{t-1} + \gamma_t^2 c_{t-1}^{\text{last}}, \qquad c_t^{\text{avg}} \;=\; \frac{C_t}{S_t + \epsilon}, \tag{43}$$

where c_{t-1}^{last} is the most recently applied clip (cached between updates). We then mix short- and long-term estimates:

$$c_t \;=\; (1-\rho) c_t^{\text{ema}} + \rho c_t^{\text{avg}}, \qquad c_t^{\text{last}} \leftarrow c_t. \tag{44}$$

This effective-time averaging reduces sensitivity to warmup length and total training steps, and prevents bias when the raw clip is computed only every K steps.

B.5. Final TrasMuon update

Substituting the components into (28) yields the final update

$$\Delta W_t \;=\; -\hat{\eta}_t \, O_t^{\text{base}} \, \text{diag}(c_t), \tag{45}$$

which preserves Muon-like directional geometry via O_t^{base} while controlling bursty magnitudes along feature axes through damping-only feature clipping c_t.

C. Convergence Analysis (Extended)

Scope. We provide a convergence *framework* for TrasMuon/energy clipping updates, separating (i) unconditional algebraic properties (bounded update norm; damping-only contraction) from (ii) mild alignment assumptions connecting the structured update to descent.

C.1. Algorithmic abstraction

Let $f : \mathbb{R}^{m\times n} \to \mathbb{R}$ and let G_t be a stochastic gradient at W_t. We study updates of the form

$$W_{t+1} \;=\; (1-\eta\lambda)\, W_t \;+\; \Delta W_t, \qquad \Delta W_t \;:=\; -\hat{\eta}_t U_t, \qquad U_t := O_t^{\text{base}} \text{diag}(c_t), \tag{46}$$

with RMS-calibrated step size

$$\hat{\eta}_t \;=\; \eta \cdot \frac{\sqrt{mn}}{\|O_t^{\text{base}}\|_F + \epsilon}, \tag{47}$$

and damping-only clipping

$$0 < c_{\min} \le c_{t,j} \le 1 \quad \forall j, t. \tag{48}$$

C.2. Deterministic algebraic properties

Lemma C.1 (Damping-only contraction)**.** *For any $A \in \mathbb{R}^{m\times n}$ and any $c \in [0,1]^n$, $\|A\,\text{diag}(c)\|_F \le \|A\|_F$.*

Proof. $\|A\,\text{diag}(c)\|_F^2 = \sum_{j=1}^n c_j^2 \|A_{\cdot j}\|_2^2 \le \sum_{j=1}^n \|A_{\cdot j}\|_2^2 = \|A\|_F^2$. □

Lemma C.2 (Row-wise RMS calibration)**.** *Under (46)–(48), for all t,*

$$\|\Delta W_t\|_F \le \eta\sqrt{mn}. \tag{49}$$

Proof. By Lemma C.1, $\|U_t\|_F = \|O_t^{\text{base}}\text{diag}(c_t)\|_F \le \|O_t^{\text{base}}\|_F$. Thus

$$\|\Delta W_t\|_F = \hat{\eta}_t \|U_t\|_F \le \eta\sqrt{mn} \cdot \frac{\|O_t^{\text{base}}\|_F}{\|O_t^{\text{base}}\|_F + \epsilon} \le \eta\sqrt{mn}.$$

□

C.3. Assumptions for descent

Assumption C.3 (L-smoothness)**.** f is L-smooth with respect to Frobenius norm: $\|\nabla f(X) - \nabla f(Y)\|_F \le L\|X - Y\|_F$.
Assumption C.4 (Stochastic gradients)**.** $\mathbb{E}[G_t \mid W_t] = \nabla f(W_t)$ and $\mathbb{E}[\|G_t - \nabla f(W_t)\|_F^2 \mid W_t] \le \sigma^2$.
Assumption C.5 (Alignment on the realized update)**.** There exists $\mu_\Delta > 0$ such that for all t,

$$\mathbb{E}\big[\langle \nabla f(W_t), \Delta W_t\rangle \mid W_t\big] \;\le\; -\mu_\Delta\, \eta\, \|\nabla f(W_t)\|_F^2, \tag{50}$$

where $\Delta W_t = -\hat{\eta}_t U_t$.

C.4. Expected stationarity

Lemma C.6 (Smoothness descent)**.** *Under Assumption C.3, for any* Δ*,*

$$f(W_t + \Delta) \le f(W_t) + \langle \nabla f(W_t), \Delta\rangle + \frac{L}{2}\|\Delta\|_F^2. \tag{51}$$

Theorem C.7 (Expected stationarity for RMS-calibrated, damping-only updates)**.** *Assume C.3 and C.5 with* $\lambda = 0$*. Then for any* $T \ge 1$*,*

$$\frac{1}{T}\sum_{t=0}^{T-1} \mathbb{E}\|\nabla f(W_t)\|_F^2 \;\le\; \frac{\mathbb{E}[f(W_0)] - f^\star}{\mu_\Delta\, \eta\, T} \;+\; \frac{L}{2\mu_\Delta}\, \eta\, mn, \tag{52}$$

where $f^\star = \inf_W f(W)$.

Proof. Apply Lemma C.6 with $\Delta = \Delta W_t$, take conditional expectation, use Assumption C.5, and bound $\|\Delta W_t\|_F^2$ by Lemma C.2. Sum over $t = 0, \dots, T-1$ and telescope $f(W_t)$. □

C.5. Extensions: weight decay, stochasticity, and PL

Weight decay. Decoupled weight decay can be handled by analyzing $f_\lambda(W) = f(W) + \frac{\lambda}{2}\|W\|_F^2$ or treating $(1 - \eta\lambda)W_t$ as an additional contraction term.

Stochastic gradients. Under Assumption C.4, the bound acquires an additional $\mathcal{O}(\eta\sigma^2)$ term as in standard SGD analyses.

PL / strong convexity. If f satisfies the PL condition, one obtains linear-type convergence to an $\mathcal{O}(\eta mn)$ (or $\mathcal{O}(\eta\sigma^2)$) neighborhood.

D. Additional Results: Language-Model Pretraining

Scope. This appendix provides supplementary visualizations for language-model pretraining and a minimal replication check. The intent is *not* to introduce new claims beyond the main text, but to (i) document late-stage behavior under the fixed training budget and (ii) reduce the risk that qualitative trends are specific to a single random seed.

Fixed-budget protocol (identical across optimizers). All runs follow the same fixed-budget protocol as Section 4.1. Training starts from random initialization and proceeds for 1500 optimization steps on FineWeb-Edu with sequence length 1024 and global batch size 1024, thereby fixing the token budget across optimizers. A single fixed learning rate $\eta = 0.0036$ and weight decay $\lambda = 0.005$ are used for all optimizers, with no learning-rate sweep and no optimizer-specific retuning in this appendix. Two schedule variants are reported: (i) a warmup–stable–decay schedule with 10% warmup and a final 20% decay phase, and (ii) the same schedule without warmup.

Metrics. Training loss is reported as a high-resolution indicator of early-stage optimization dynamics and stability under an identical training budget. This appendix presents the corresponding loss trajectories to complement the main-text summaries.

D.1. Qwen3-0.6B: Late-stage loss under a fixed 1500-step budget

The late-stage training window (steps 1200–1500) is examined to complement the early-stage analysis in the main text. Figure 6 shows the corresponding loss trajectories in this window for both schedule variants. These curves document late-stage behavior under a fixed training budget and are not intended to imply full convergence.

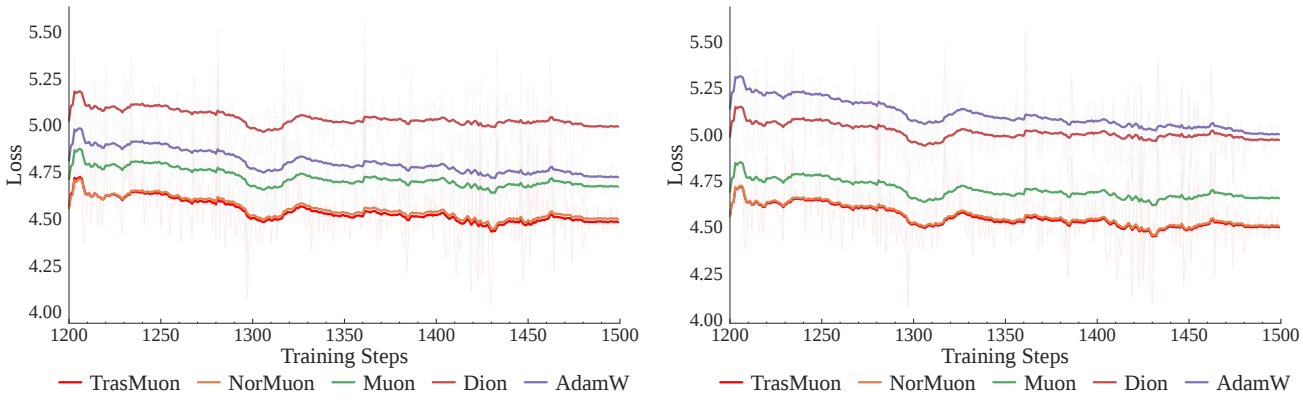

(a) Warmup-enabled. *(b)* Warmup-free.

Figure 6. **Qwen3-0.6B late-stage window (steps 1200–1500) under a fixed-budget protocol.** Training loss under warmup-enabled vs. warmup-free variants of the same warmup–stable–decay schedule with a final decay phase near the end of training.

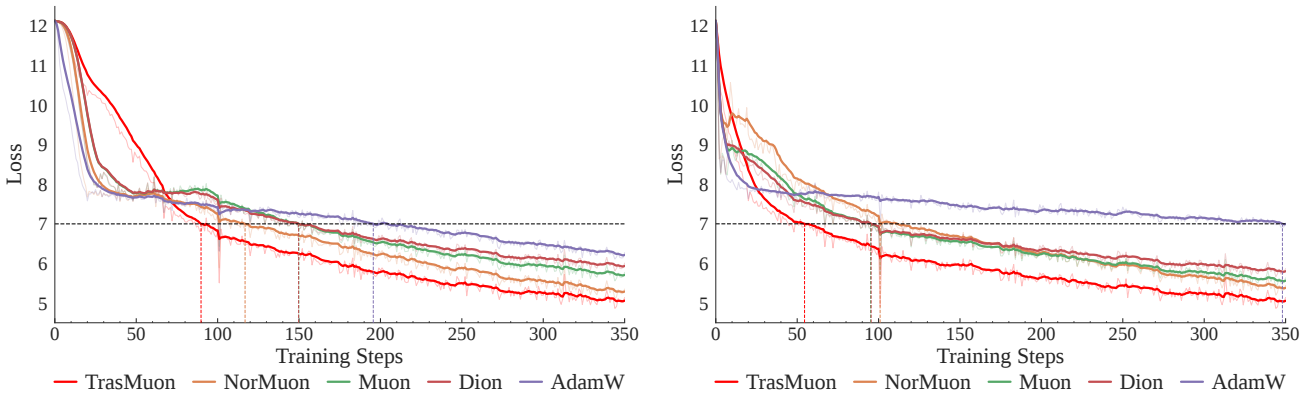

(a) Warmup-enabled, seed 42. *(b)* Warmup-free, seed 42.

Figure 7. **Qwen3-0.6B replication under an identical protocol (additional seed).** Early-stage training loss (steps 0–350) for an additional random seed, under the same configuration as the main-text experiment.

D.2. Qwen3-0.6B: Minimal replication check

The main text reports Qwen3-0.6B results under a single fixed seed. To reduce the possibility that the observed qualitative trends are specific to that particular random draw, the same Qwen3-0.6B runs are repeated with an additional random seed while keeping *all* other settings identical, including the data pipeline, token budget, model architecture, learning rate, weight decay, and schedule variant. These replication runs are not used for hyperparameter tuning and are included solely as a robustness check under an identical protocol.

Figure 7 presents early-stage loss trajectories over steps 0–350 for the additional seed. Across both schedule variants, the qualitative optimizer behavior remains consistent with the main-text observations. No claim of statistical significance is made from this minimal replication; the results are provided as supplementary evidence of qualitative robustness under matched conditions.

D.3. GPT-2 Small: Additional architecture under the same protocol

GPT-2 Small is additionally evaluated under the same fixed-budget protocol to assess whether the observed qualitative dynamics transfer to a different architecture. Figure 8 presents early-stage loss trajectories over steps 0–350 for both schedule variants, and Figure 9 reports the late-stage window over steps 1200–1500. These plots are included to complement the main-text results, and the late-stage window is reported for completeness rather than as evidence of full convergence.

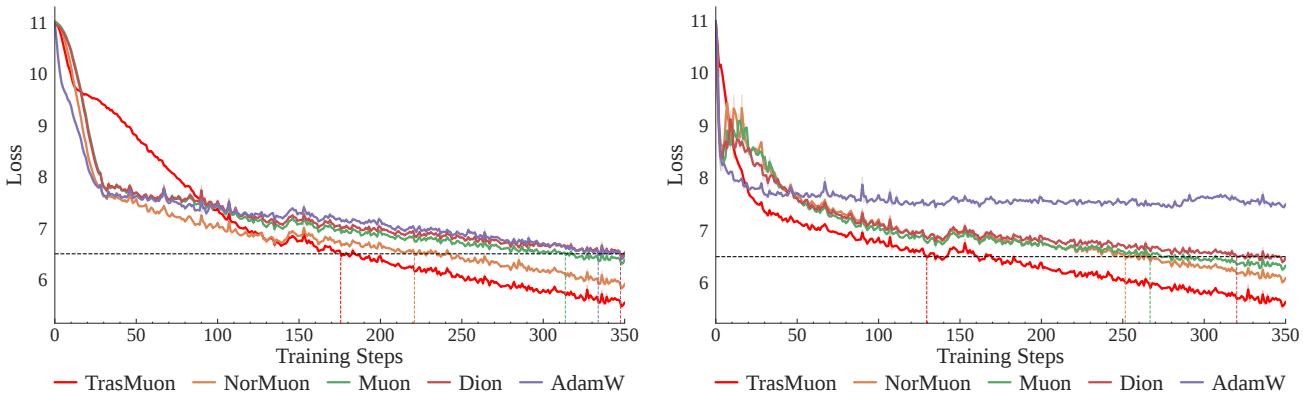

(a) Warmup-enabled. *(b)* Warmup-free.

Figure 8. **GPT-2 Small early-stage dynamics (steps 0–350) under a fixed-budget protocol.** Warmup-enabled vs. warmup-free variants of the same warmup–stable–decay schedule.

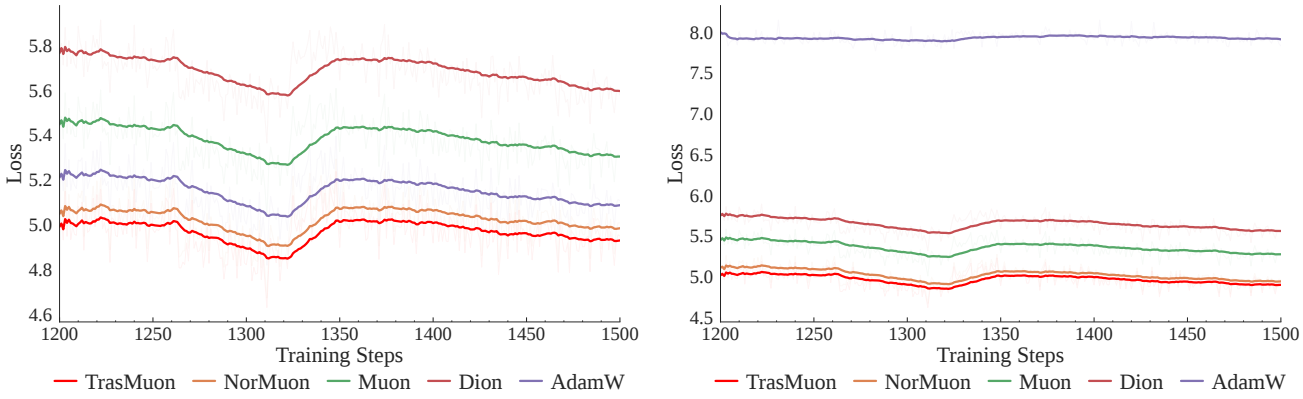

(a) Warmup-enabled. *(b)* Warmup-free.

Figure 9. **GPT-2 Small late-stage window (steps 1200–1500) under a fixed-budget protocol.** Training loss for warmup-enabled vs. warmup-free schedule variants.

E. Additional Vision Transformer Experiments

E.1. ImageNet-100 Data Source and Construction

To reduce dataset preparation overhead, we use a publicly available ImageNet-100 *image archive* hosted on Kaggle (Ambityga, 2021) as a convenient storage source. Importantly, the Kaggle archive is used *only* as a source of image files. Class membership and the train/validation split are defined strictly according to the ILSVRC-2012 (ImageNet-1k) specification. Concretely, we select a fixed subset of 100 ILSVRC-2012 classes (specified by synset IDs) and retain only images whose labels match these synsets; we then follow the standard ILSVRC-2012 train/validation split. As a sanity check, we verify (in code) the synset-to-index mapping, per-class image counts, and that no images outside the selected synsets are included. This ensures that the benchmark corresponds to a well-defined subset of ImageNet-1k, independent of the hosting platform.

E.2. ImageNet-100 Experimental Protocol and Seed Allocation

We evaluate optimization methods on ImageNet-100 using a ViT-Base/16 architecture at 224×224 resolution. Training follows a standard ViT/DeiT recipe (Dosovitskiy et al., 2021; Touvron et al., 2021), including random resized cropping, horizontal flipping, color jitter, RandAugment, and random erasing, together with label smoothing and Mixup (CutMix disabled).

Weight decay is applied with parameter grouping: LayerNorm and bias parameters use zero weight decay, and all remaining parameters use a fixed decay rate. Unless otherwise stated, all experiments use a base learning rate of 1×10^{-3} and a weight

Table 2. **ViT on ImageNet-100.** Final *validation* top-1 accuracy (mean ± standard deviation) over three random seeds (42, 43, 44).

Optimizer	Accuracy Mean	Accuracy Std
TrasMuon	**77.47%**	**0.34%**
NorMuon	77.10%	0.21%
Muon	69.69%	0.08%
AdamW	42.53%	4.38%

Table 3. **ViT on CIFAR-100 with column-localized gradient bursts.** Final top-1 test accuracy (mean ± standard deviation) over three seeds (42, 43, 44).

Optimizer	Accuracy Mean	Accuracy Std
TrasMuon	**58.77%**	**0.22%**
NorMuon	58.31%	0.52%
Muon	57.48%	0.52%
AdamW	35.03%	5.05%

decay of 5×10^{-2}. We compare AdamW (Loshchilov & Hutter, 2019), Muon (Jordan et al., 2024), NorMuon (Li et al., 2025), and TRASMUON under the same model architecture, data pipeline, training schedule, and compute budget, using three random seeds (42, 43, 44). Optimizer-specific parameters follow the respective published defaults and our unified implementation. For each method, we report the mean and standard deviation of *validation* top-1 accuracy across seeds (Table 2).

E.3. CIFAR-100: Column-Energy Stress Test

Setup (stress-test benchmark). We conduct a controlled stress test on CIFAR-100 using a Vision Transformer to assess optimizer robustness under axis-localized nonstationarity. Unless otherwise specified, all runs use 30 epochs, batch size 128, learning rate 1×10^{-3}, weight decay 5×10^{-3}, and identical data loading and preprocessing. We report mean and standard deviation of test accuracy over three random seeds (42, 43, 44).

Burst injection. To introduce structured nonstationarity without changing the data distribution, we inject sparse *column-localized gradient bursts* into selected large 2D parameter matrices (attention and MLP projections). The goal of this protocol is not to claim that injected bursts match the exact distribution of naturally occurring outliers, but to provide a reproducible mechanism-level stressor that concentrates energy along a small subset of feature axes. Crucially, the same burst pattern (targeted layers, selected columns, and timesteps) is applied across optimizers by fixing the burst random seed, enabling direct, fair comparison of optimizer responses. Full implementation details are provided in Appendix E.4.

Observed behavior. Table 3 summarizes test accuracy under burst injection. Across this stress setting, Muon-family optimizers maintain higher accuracy and lower variability than AdamW. Normalization-based variants reduce variance relative to Muon, while TRASMUON attains the highest mean accuracy and the smallest spread across seeds in this configuration.

E.4. Burst Injection Protocol

We define a column-wise gradient burst operator applied to selected 2D weight matrices to induce controlled column-energy spikes without altering the data distribution. At each burst step, we select k column indices (random or fixed, as specified) and perturb each selected column by adding a normalized random direction:

$$g_{:,j} \leftarrow g_{:,j} + \alpha \cdot \frac{u}{\|u\|_2 + \epsilon}, \quad u \sim \mathcal{N}(0, I).$$

The amplitude α can be specified as a fixed absolute value or scaled relative to the current gradient magnitude using a Frobenius-normalized reference:

$$\alpha = \rho \cdot \frac{\|g\|_F}{\sqrt{d_{\text{out}} d_{\text{in}}}},$$

Table 4. ROI patch pool used for random ROI events (rectangles are $[x_0, x_1] \times [y_0, y_1]$).

ROI patches
Corners: $[0.00, 0.03] \times [0.00, 0.03]$, $[0.97, 1.00] \times [0.00, 0.03]$, $[0.00, 0.03] \times [0.97, 1.00]$, $[0.97, 1.00] \times [0.97, 1.00]$
Edges: $[0.48, 0.53] \times [0.00, 0.05]$, $[0.48, 0.53] \times [0.95, 1.00]$, $[0.00, 0.05] \times [0.48, 0.53]$, $[0.95, 1.00] \times [0.48, 0.53]$
Interior: $[0.20, 0.25] \times [0.20, 0.25]$, $[0.45, 0.50] \times [0.10, 0.15]$, $[0.10, 0.15] \times [0.55, 0.60]$, $[0.60, 0.65] \times [0.60, 0.65]$

optionally clipped by a maximum threshold. Bursts occur every T optimization steps after an optional warmup phase and target only designated 2D layers (e.g., attention projections and MLP weights). Burst events and optimizer internal statistics (including feature-wise clipping coefficients, when applicable) are logged at the same timesteps to enable direct alignment between perturbations and optimizer responses.

F. Additional PINN Details: Random-ROI Sampling Stress Test

Task recap. We consider the Helmholtz equation on $\Omega = [0, 1]^2$ with homogeneous Dirichlet boundary conditions and a manufactured solution $u^\star$ (see Section 4.3 for the PDE, loss definition, and the relL_2 metric). This appendix specifies the non-stationary sampling protocol used to stress-test optimizer robustness under controlled distribution shifts.

Training configuration. We use an MLP with hidden dimensions $(128, 128, 128)$ and $\tanh$ activation, trained for 4000 steps. At each step we sample $N_r = 1024$ interior points and $N_b = 256$ boundary points with boundary weight $\lambda_b = 100$. We evaluate every 200 steps on a fixed 128×128 grid.

ROI sampling as a distribution shift. Starting from step $t_0 = 1000$, we trigger ROI events every $K_{\text{out}} = 20$ steps. At an ROI event step t, we sample interior points from a mixture distribution

$$p_t(x) \;=\; (1 - \alpha)\, p_0(x) + \alpha\, p_{\text{roi}}^{(t)}(x), \qquad \alpha = 0.95, \tag{53}$$

where p_0 is uniform over Ω and $p_{\text{roi}}^{(t)}$ is uniform over the selected ROI patch $\Omega_{\text{roi}}^{(t)}$. This produces a controlled, non-stationary sampling distribution (a stressor analogous to adaptive/ROI refinement in practical PINNs).

Random ROI patch pool (reproducible). The ROI patch $\Omega_{\text{roi}}^{(t)}$ is selected from a fixed pool (Table 4) using a deterministic `step_hash` seeding rule. Thus ROI locations vary across events yet remain fully reproducible given the experiment configuration and training step index.

ROI-local evaluation. To quantify local disturbance and recovery, at ROI event steps we additionally compute an ROI-local relL_2 on a 64×64 grid restricted to $\Omega_{\text{roi}}^{(t)}$, and estimate non-ROI error by sampling 4096 points from $\Omega \setminus \Omega_{\text{roi}}^{(t)}$. These diagnostics separate global convergence from localized behavior under distribution shifts.

F.1. Step-Size Alignment and Learning-Rate Sensitivity (PINN Helmholtz, $k = 2$)

Motivation. Nominal learning rates are not directly comparable across update rules because different optimizers can induce different *effective* parameter-space step magnitudes. To reduce the confound that performance differences are driven by trivial step-size mismatches, we complement the main comparison with (i) a short step-size alignment diagnostic and (ii) a shared learning-rate (LR) sweep.

Step-size alignment diagnostic. Figure 10a reports the achieved effective step size, computed from parameter differences during an initial stationary window (before any ROI perturbations are introduced),

$$s_t \;=\; \frac{\|\Delta\theta_t\|_2}{\sqrt{P}}, \qquad P = \dim(\theta).$$

We target a fixed reference magnitude (dashed line) with a tolerance band (shaded region). Muon and TRASMUON attain comparable achieved step sizes within the tolerance range, supporting that subsequent robustness comparisons are not explained by a simple global step-size discrepancy.

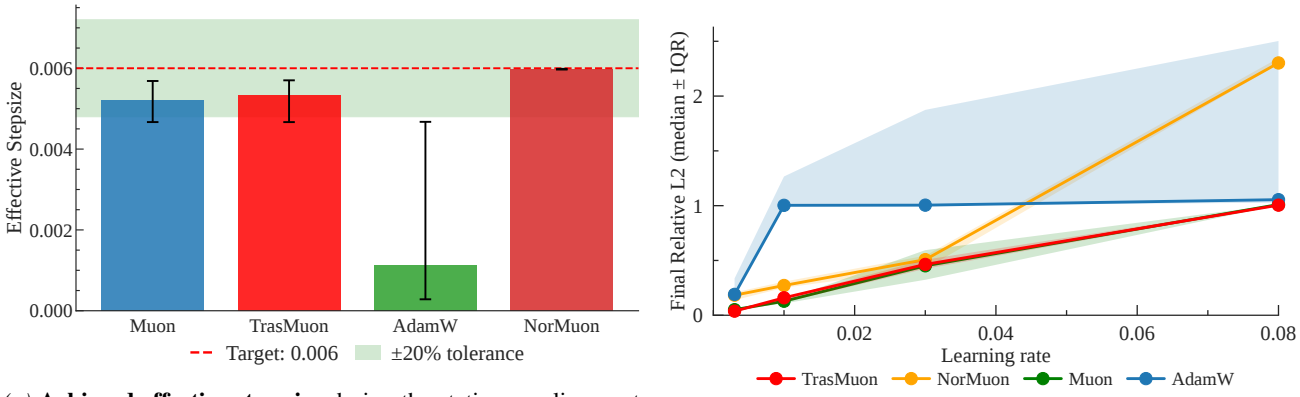

(a) **Achieved effective step size** during the stationary alignment window (before ROI events). The dashed line is the target, and the shaded region indicates tolerance. Error bars denote variability across seeds.

(b) **LR sensitivity** of final relative L_2 error under a shared LR sweep. Lines show the median across seeds and shaded bands indicate the IQR.

Figure 10. **PINN Helmholtz ($k = 2$): step-size alignment and LR sensitivity.** (a) Effective step-size alignment reduces trivial magnitude confounds when comparing optimizers with different update rules. (b) A shared LR sweep summarizes sensitivity to step-size calibration via final relative L_2 error.

Learning-rate sweep. Figure 10b shows the final relative L_2 error under a shared LR sweep. Shaded bands summarize variability across random seeds (median with an interquartile range). Both methods exhibit the expected degradation as LR increases beyond the stable region. Together with the alignment diagnostic, this sweep provides a complementary view of optimizer sensitivity to step-size calibration under the same training and sampling protocol.

F.2. Additional PINN Diagnostics: Metric Distributions Across Seeds

We visualize the distribution of key robustness and accuracy metrics across random seeds for the PINN Helmholtz benchmark($k = 2$). This figure serves as a distributional check to ensure that the reported trends are not driven by a single favorable run.

G. Supplementary Details for the Mechanistic Study

This appendix provides protocol-level details and supporting evidence for the mechanistic study in Section 4.4. The intent is two-fold: (i) to make the stress protocol fully reproducible, and (ii) to document a minimal, time-aligned evidence chain that is *consistent with* the intended energy-indexed, feature-wise clipping mechanism under a controlled intervention. We do not introduce new claims beyond Section 4.4.

G.1. Reproducible protocol

Quadratic objective and stiffness. We optimize a matrix parameter $W \in \mathbb{R}^{d\times d}$ under

$$f(W) \;=\; \tfrac{1}{2}\|AWB - T\|_F^2, \tag{54}$$

where $A = U\Sigma_A U^\top$ and $B = V\Sigma_B V^\top$. Here U, V are orthogonal matrices and Σ_A, Σ_B are diagonal spectra constructed to achieve a target condition number $\kappa \in \{10^2, 10^4, 10^6\}$. We repeat each configuration over multiple random seeds/rotations and report robust statistics (median and IQR).

Column-localized burst injection (controlled intervention). Every K_{out} steps we inject an outlier event by amplifying a small subset of momentum columns. Concretely, we sample $\mathcal{J} \subseteq [d]$ with $|\mathcal{J}| = s \ll d$ and apply

$$\widetilde{M}_{t,\cdot j} \;=\; \begin{cases} a\, M_{t,\cdot j}, & \text{if } j \in \mathcal{J}, \\ M_{t,\cdot j}, & \text{otherwise,} \end{cases} \qquad a > 1, \tag{55}$$

then form the optimizer update at that step using $\widetilde{M}_t$ in place of M_t. This intervention changes the *optimization dynamics* but keeps the underlying objective $f(W)$ unchanged.

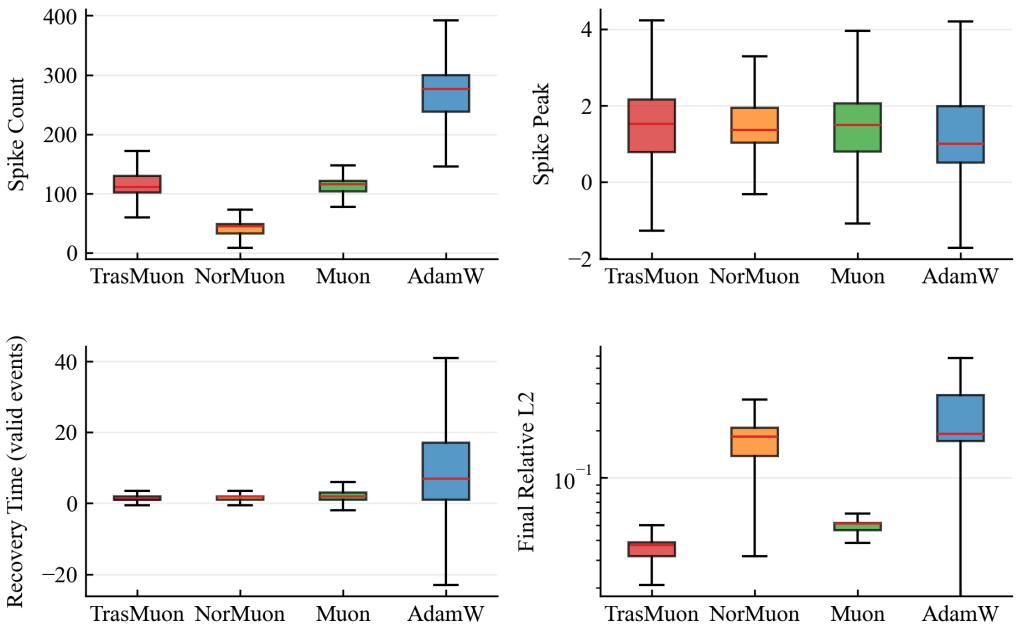

Figure 11. **PINN Helmholtz($k = 2$): metric distributions across seeds.** Boxplots summarize spike count, spike peak, recovery time (valid events), valid-event rate, and final relative L_2 error across seeds under the same training protocol. Each box shows the median and interquartile range (IQR); whiskers indicate the remaining spread.

Preserving vs. breaking feature/column semantics (`fix_V`). Feature-wise clipping is axis-aligned (column-wise), so its effect depends on whether the chosen column axis remains meaningful. In the main setting (`fix_V=True`), we preserve the column basis used for burst injection, so "columns" correspond to consistent feature axes across training and injected events. As a boundary condition (`fix_V=False`), we apply an additional orthogonal mixing in column space, so injected energy is dispersed across columns; in this case, selective column-wise clipping is not expected to provide the same advantage.

G.2. Minimal evidence chain (time-aligned observables)

Section 4.4 argues that spike suppression is consistent with the following ordering under a controlled intervention: *outlier injection → relative energy increases → stronger applied clipping → reduced loss spikes*. We summarize the corresponding observables, which are directly logged and visualized in Fig. 5.

(1) Outlier injection increases relative energy. Eq. (55) increases the column energies $E_{t,j} = \sum_i \widetilde{M}^2_{t,ij}$ for $j \in \mathcal{J}$. We track the relative energy ratio

$$r_{t,j} \;=\; \frac{E_{t,j}}{E_t^{\mathrm{ref}} + \epsilon}, \tag{56}$$

where E_t^{ref} is the running reference used by TRASMUON. We visualize robust summaries such as r_{q95} and $r_{\max}$, which rise at injected outlier steps (Fig. 5, top).

(2) Higher relative energy is followed by stronger applied clipping. TRASMUON produces damping-only clipping coefficients $c_{t,j}^{\mathrm{used}} \in [c_{\min}, 1]$ that decrease with $r_{t,j}$. Consistent with this design, outlier steps are followed by a decrease in the applied signal, visible via $c_{\mathrm{used,min}} = \min_j c_{t,j}^{\mathrm{used}}$ (Fig. 5, bottom). This time alignment is consistent with the intended ordering "energy rise → clipping increase" under the intervention.

(3) Applied clipping attenuates column updates (selectively). Given the matrix-form update,

$$\Delta W_t \;=\; -\,\hat{\eta}_t\, O_t^{\mathrm{base}}\, \mathrm{diag}(c_t^{\mathrm{used}}), \tag{57}$$

each column update magnitude is scaled by $c_{t,j}^{\mathrm{used}}$:

$$\|\Delta W_{t,\cdot j}\|_2 \;=\; c_{t,j}^{\mathrm{used}}\;\hat{\eta}_t\;\|O_{t,\cdot j}^{\mathrm{base}}\|_2 \;\le\; \hat{\eta}_t\;\|O_{t,\cdot j}^{\mathrm{base}}\|_2. \tag{58}$$

Thus clipping is *selective*: only columns with $c_{t,j}^{\mathrm{used}} < 1$ are damped, while the structured direction O_t^{base} is preserved.

(4) Spike suppression and objective improvement. Consistent with (1)–(3), TRASMUON reduces loss spikes around outlier events (Fig. 4) and achieves lower final objective values than the backbone under matched compute (Table 1). Spike metrics (count/peak) are computed using the same deterministic detection rule across methods; details are provided in our experiment scripts and plotting utilities.

Controls that break the chain. We include two controls that remove key requirements of the mechanism: (i) TRASMUON-NOCLIP sets $c_t^{\mathrm{used}} \equiv \mathbf{1}$, removing the attenuation in Eq. (58); empirically it behaves similarly to NorMuon (Table 1). (ii) Under `fix_V=False`, the injected energy is dispersed across columns, so clipping is no longer aligned with injected directions; correspondingly, the advantage of feature-wise clipping diminishes (Table 5).

Table 5. **Toy-2 boundary condition (`fix_V=False`).** When feature/column semantics are broken by column-space mixing, the advantage of feature-wise clipping diminishes.

Method	Spike Count	Final Loss
NorMuon	79 (74,86)	**1.1e+06** (8.4e+05,1.6e+06)
TRASMUON-noClip	80 (74,87)	1.4e+06 (9.8e+05,1.7e+06)
TRASMUON-clip-only	74 (67,80)	1.5e+06 (1.2e+06,1.8e+06)
TRASMUON-clip+SF	**72** (65,80)	1.3e+06 (9.4e+05,1.7e+06)